Peer-reviewed version available at Micromachines 2017, 8, 31; doi:10.3390/mi8020031

Article

A MEMS Device for Quantitative *in situ* Mechanical Testing in Electron Microscope

Xiaodong Wang[1,2], Shengcheng Mao[1,*], Jianfei Zhang[1], Zhipeng Li[1], Qingsong Deng[1], Jin Ning[3], Xudong Yang[4], Li Wang[1], Yuan Ji[1], Xiaochen Li[1], Yinong Liu[5,*], Ze Zhang[1,6] and Xiaodong Han[1,*]

1 Beijing Key Lab of Microstructure and Property of Advanced Materials, Beijing University of Technology, Beijing 100124, China; wangxiaodongfy@163.com, maoshengcheng@163.com, 344900115@qq.com, lizhipeng1111@yeah.net, qsdeng@bjut.edu.cn, liw@bjut.edu.cn, jiyuan@bjut.edu.cn, xiaochen_lee@foxmail.com, xdhan@bjut.edu.cn

2 Department of Fundamental Sciences, Chinese People's Armed Police Force Academy, Langfang 065000, China; wangxiaodongfy@163.com

3 Research Center of Engineering for Semiconductor Integrated Technology, Institute of Semiconductors, Chinese Academy of Sciences, Beijing 100083, China; ningjin@semi.ac.cn

4 College of electronic information and control engineering, Beijing University of Technology, Beijing 100124, China; yangliuge@bjut.edu.cn

5 School of Mechanical and Chemical Engineering, The University of Western Australia, Crawley, 6009 WA, Australia, yinong.liu@uwa.edu.au

6 State Key Laboratory of Silicon Materials and Department of Materials Science and Engineering, Zhejiang University, Hangzhou 310008, China, zezhang@zju.edu.cn

* Correspondence: maoshengcheng@163.com, Tel.: +86-10-6739-6769; yinong.liu@uwa.edu.au, Tel.: +61-8-6488-3132; xdhan@bjut.edu.cn, Tel.: +86-10-6739-6087

Abstract: In this work, we designed a MEMS device which allows simultaneous direct measurement of mechanical properties during deformation under external stress and characterization of the evolution of microstructure of nanomaterials within a transmission electron microscope. This MEMS device makes it easy to establish the correlation between microstructure and mechanical properties of nanomaterials. The device uses piezoresistive sensors to qualitatively measure the force and displacement of nanomaterials, e.g., in wire and thin plate forms. The device has a theoretical displacement resolution of 0.19 nm and a force resolution of 2.1 μN. The device has a theoretical displacement range limit of 2.74 μm and a load range limit of 27.75 mN.

Keywords: piezoresistive sensor, electron microscope, *in situ* mechanical test

1. Introduction

Mechanical properties of materials are strongly influenced by their microstructures. Materials often show special mechanical properties compared to its bulk counterparts when the grain size or physical dimension is reduced to nanometer scale [1-8]. For example, brittle Si and SiC show super-plasticity when their sizes are reduced to below ~100 nanometers [9-13]; the elasticity of nanosized copper can approach the theoretical elastic strain limit [14]; the martensitic transformation can be completely suppressed in NiTi shape memory alloys when the sample thickness is below ~50 nm [15, 16]. In this regard, it is important to develop capabilities to allow quantitative studies of the structure-property correlations of materials at the nano and atomic scales.

Many techniques and devices, adapted to scanning electron microscopes (SEM) or transmission electron microscopes (TEM), have been designed to allow *in situ* studies of structure-property relationships at the nano and atomic scales [12, 17-26]. Some devices allow observation of the microstructural evolution and simultaneous measurement of stress-strain curves, thus give us an opportunity to understand the microscopic mechanisms of deformation and to better guide the development of new materials [27, 28]. Techniques currently available for mechanical testing at nano

scale include nanoindentation [29], bugling [30], resonance [31], bending [32] and micro-tensile testing [33] using micro/nanosized samples in SEM, TEM and atomic force microscope (AFM). For TEM *in situ* analysis, one main functional requirement of the technique for structure-property correlations studies is to quantitatively measure the stress-strain behavior of the sample in TEM whilst having negligible impact on the double-axis tilt of the TEM sample holder. Nanoindentation has been adapted in TEM for *in situ* deformation measurement [34]. Nanoindentation has high displacement and force resolutions of 0.03 nm and 0.1 μN [35], which is commonly used to determine elastic modulus, hardness, and stiffness of the surface of materials [36-41]. However, this technique places the displacement and force sensors at the end of the TEM holder, thus prohibits the β-axis tilt and partially limits the orientation capability of TEM.

Recently, MEMS-based devices, integrating actuators, sensors and signal processing circuits in a small volume of a few millimeters or even micrometers at the head of TEM holder, have been developed for studies the structure-property relationships at the atomic scale [42-44]. To accurately measure the mechanical property of nanosized materials, the resolutions of the displacement and force sensors need to be up to the order of tens of nanometers and micro-newtons, respectively. Displacement and force can be determined in electron microscopes mainly through two methods, imaging and capacitance. The imaging method determines the displacement by measuring the displacement difference of two flexible beams in TEM/SEM. The load is then given as the product of the displacement of the force sensor beam and the spring constant of the beam [45, 46]. By using the imaging method, it is unable to output the stress-strain curve of the specimen in real time. For the capacitance method, the displacement and force are measured based on the capacitance variances upon deformation of the sensors located at the roots of the beams. The capacitance method has been widely used in harsh environment because of its superior properties, such as small temperature drift, low power consumption, well process compatibility and direct output of the signals [47]. Differential capacitance based sensors have high force and displacement resolutions [27, 48, 49] but have comparatively larger sizes, thus can only be used in single-tilt or small angle double-tilt TEM holders and are difficult to use for atomic scale microstructural analysis.

Piezoresistive sensors, fabricated with semiconductor materials, have the advantages of easy fabrication, small size and high sensitivity [50], thus are a good candidate for double-tilt TEM holders. The operating principle of piezoresistive sensors is that the resistance of the piezoresistive sensor varies with external stress/strain. The electric signals of the resistance can be directly read out using a Wheatstone bridge circuit, which is small in size and can be integrated with the sensor using MEMS technique. Because of its small size, a piezoresistive sensor can be easily placed on simple structures such as cantilever and clamped beams [49]. In order to improve their sensitivity, piezoresistors were fabricated on the surface of the beam perpendicular to the force direction in many cases. Force resolution of piezoresistive sensors has been reported to be as small as nano-newtons [51], implying a possibility to measure the mechanical properties of nanosized materials. However, no MEMS-based devices with piezoresistive sensors for structure-property studies at the nano/atomic scale seem to have been developed.

In this work, we designed a piezoresistive sensor based MEMS device for mechanical deformation with a displacement resolutions of 7 nm and a force resolution of 2.2 μN. The device is small in size and has a potential to be adapted in SEM/TEM for quantitative uniaxial tensile testing of samples with thickness smaller than 100 nm and width of hundreds of nanometers. Aluminum thin film sample with thickness of 510 nm was subjected to trial test the device in SEM to validate its effectiveness.

2. Mechanical testing system

2.1. Description of the system

Fig. 1 shows a schematic of the design of the testing system. Its operation control is given in Fig. 1(a). The system comprises an actuation system, a MEMS device, two single-system-power suppliers and two digital multimeters (6½ digit). The two single-system-power suppliers provide DC operating voltage for the two piezoresistive sensors. Beams on the device was driven by a piezoceramic actuator with a travel distance of 100 μm and a minimum step of 7 nm. Two digital mulitmeters were used to collect the output voltages of the sensors.

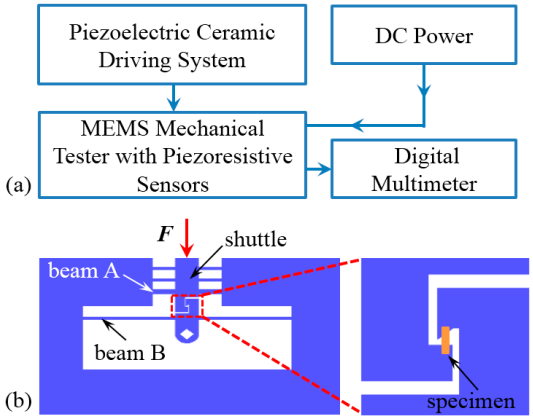

Figure 1. Schematic of the testing system in SEM: (a) The actuation control flow chart; (b) Design of the testing apparatus.

The MEMS device was fabricated using bulk silicon microfabrication process, and the design is illustrated in Fig. 1b. Two sensors, A and B, were placed on two beams, A and B, to measure the displacement and force. Sensor A was placed at the root of beam A to measure the deflection of the center of beam A. In order to maintain the stability of sensor A, two more clamped beams parallel to beam A were connected with beam A by a shuttle, as can be seen in Fig. 1b. Sensor B was placed at the root of beam B, which is longer than beam A, to measure the deflection of beam B. The deformation strain of the specimen is calculated using equation (1):

$$\varepsilon = \frac{x_a - x_b}{l_0} \tag{1}$$

where x_a and x_b are the center deflections of beams A and B respectively and l_0 is the initial length of the specimen.

The load applied on the specimen approximately equals to the driving force acting on the beam center, which was calculated based on the deflection of beam B. The stress is given as follows:

$$\sigma = \frac{F_b}{S} \tag{2}$$

where F_b is the driving force acting on beam B and S is the cross-sectional area of the specimen. Using a push-to-pull structure, the external compressive stress was transferred to a tensile stress on the specimen, as shown in Fig. 1b.

2.2. Sensor design

Fig. 2 shows the MEMS device with two piezoresistive sensors. The overall dimensions of the device are 1.3 mm×2.4 mm×0.44 mm, thus can be easily installed on the sample stage at the head of a TEM hold. Four piezoresistors indicated as the green areas were prepared on beams A and B, as shown in the insets of Fig. 2. The four sensors form a half Wheatstone bridge, to allow precise measurement of the resistance variance. The two piezoresistors located at the roots of beams A and

B, R_1 and R_2, measure the deflection of the beam. The resistances of the other two resistors attached to the substrate, R_3 and R_4, remain constant during deflection of the beam. The four resistors are electrically connected with Al interconnects. To improve the consistency of the process and to partially compensate the influence of temperature, the resistors on the beam and those on the substrate were placed as close as possible [52]. The beams and the piezoresistors are aligned along the <110> direction on the (100) plane of a silicon wafer substrate for obtaining a better sensitivity of the sensor [53].

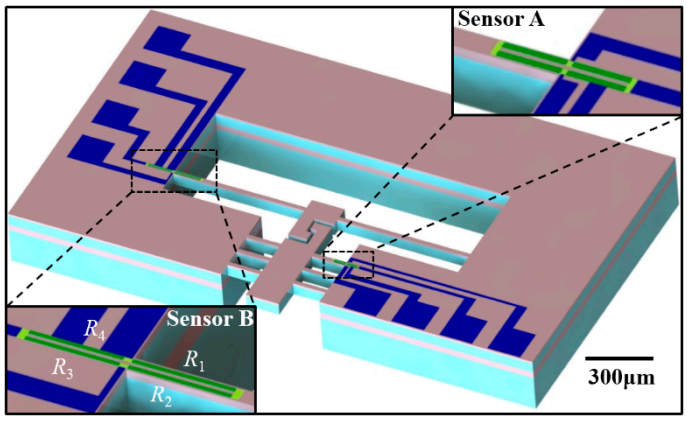

Figure 2. Sketch of the MEMS device with piezoresistive sensors.

When the clamped beams deform upon an in-plane force, stress will concentrate at the beam roots. The stress is free at the neutral plane of the beam and increases gradually with increasing distance from the neutral plane. The variance of the resistance is given in equation (3) [54]:

$$\frac{\Delta R}{R} = \pi_l \sigma_l + \pi_t \sigma_t \tag{3}$$

where σ_l and σ_t are the longitudinal and transverse stresses, and π_l and π_t are the piezoresistance coefficients along the longitudinal and transverse directions. Since σ_t is much smaller than σ_l, the $\pi_t \sigma_t$ term can be neglected [51]. Fig. 3 shows the positions of the piezoresistors on the beam and the parameters used in equation (4) and (5). In the case of small deformation, the variance of resistance can be written as:

$$\frac{\Delta R}{R} = \frac{6\pi_l E d' \omega}{L^3}\left(L - \frac{l_p}{2}\right) \tag{4}$$

where E is the Young's modulus of silicon in <110> direction, 169 GPa [55], L is the beam length, l_p is the piezoresistor length, ω is the beam center deflection, and d' is the distance between the resistor centerline and the neutral plane of the beam. The d' value can be expressed as:

$$d' = \frac{D}{2} - \frac{w_p}{2} - d'' \tag{5}$$

where D is the beam thickness (along the force direction), w_p is the width of the piezoresistor, and d'' is the distance between the outer edge of the piezoresistor and the beam. Fig. 3 shows all of the parameters in equation (5).

When a tensile stress is applied to the specimen, assuming that the piezoresistors R_3 and R_4 have an equal resistance variance of ΔR, the output voltage from the bridge is then given as:

$$V_{out} \approx \frac{\Delta R}{2R} V_B \tag{6}$$

where V_B is the bridge bias voltage.

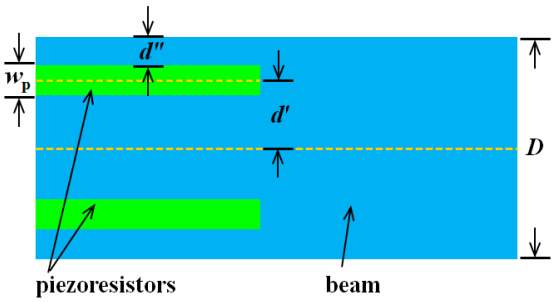

Figure 3. Schematic of the positions of the piezoresistors on the beam and the parameters used in equations (4) and (5).

The displacement sensitivity (S_D) of the piezoresistive sensors is defined as the ratio of the output voltage to the beam deflection, and is given by combining equations (4) and (6):

$$S_D = \frac{3\pi_l V_B E d'}{L^3} \quad (L - l_p) \tag{7}$$

The noise of the piezoresistive sensors arises from both intrinsic and extrinsic sources. Johnson noise and 1/f noise are the two main intrinsic noises, and their noise power spectral densities are given in equations (8) and (9), respectively [56]:

$$\overline{V_J}^2 = \frac{4k_B T l_p}{N_p q \mu_p d_p w_p}(f_{max} - f_{min}) \tag{8}$$

and

$$\overline{V_H}^2 = \frac{\alpha V_B^2}{N_p l_p d_p w_p} \ln \frac{f_{max}}{f_{min}} \tag{9}$$

where k_B is the Boltzmann constant, T is the absolute temperature, N_P is the dopant concentration, q is the amount of the carrier charge, μ_P is the hole mobility, d_P is the piezoresistor thickness, α is a non-dimensional fitting parameter depending on the annealing conditions, and f_{max} and f_{min} are the upper and lower measurement frequency limits. The displacement resolution of the sensors is defined as the ratio of the noise to the displacement sensitivity (only considering Johnson and 1/f noise), which can be written as:

$$R_D = \frac{L^3 \sqrt{\frac{4k_B T l_p}{N_p q \mu_p d_p w_p}(f_{max} - f_{min}) + \frac{\alpha V_B^2}{N_p l_p d_p w_p} \ln \frac{f_{max}}{f_{min}}}}{3\pi_l V_B E d'(L - l_p)} \tag{10}$$

Optimized design can effectively decrease the noise power and improve the displacement resolution, i.e., the smallest signal that can be detected. According to equation (10), the density of the noise power decreases with increasing of the piezoresistor's width (w_P). For a nearly constant d'', depending on the MEMS technology, the d' will become shorter when w_P is reduced, leading to a decrease in the displacement sensitivity. To obtain an optimal width ($w_{P\text{-optimal}}$), the resolution R_D can be partially differentiated against the width of the piezoresistor. The optimal width thus obtained is:

$$w_{p\text{-optimal}} = \frac{D}{3} - \frac{2}{3} d'' \tag{11}$$

According to equations (8) and (9), increase in the length of the piezoresistor, l_P, has an opposite influence on the power density of the Hooge and Johnson noises, i.e., decrease in the Hooge noise but increase in the Johnson noise. It is further noted from equation (7) that increase in the l_P can also lead to a loss in displacement sensitivity. Because of the complicated effect of the l_P on the displacement resolution and sensitivity, the resolution was partially differentiated against the l_P to obtain an optimal length contributing to a high resolution. For each clamped beam length, L, an

optimal $l_{\text{p-optimal}}$ is obtained. Fig. 4 shows the evolution of $l_{\text{p-optimal}}/L$ as a function of the clamped beam length. The results show that the $l_{\text{p-optimal}}/L$ decreases with increasing L.

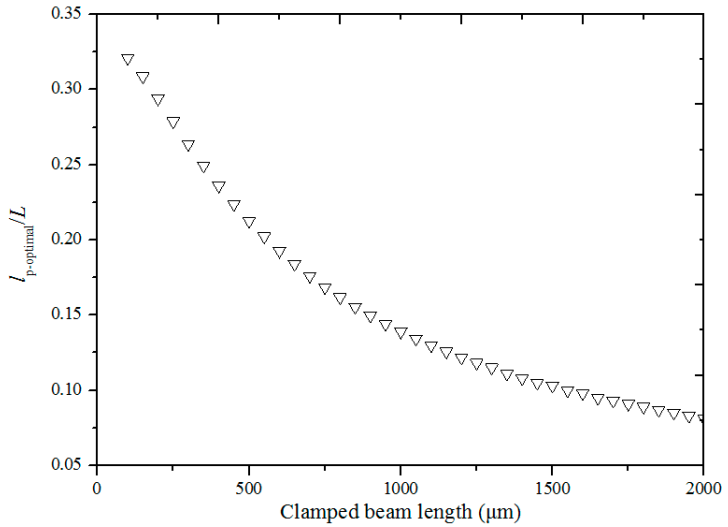

Figure 4. Evolution of the $l_{\text{p-optimal}}/L$ as a function of the clamped beam length (L).

Table 1. Parameters of the two piezoresistive sensors.

Parameters	Value		Unit
	Sensor A	Sensor B	
α	10^{-5}		-
T	300		K
μ_p	0.934×10^{-2}		$cm^2 \cdot V^{-1} \cdot s^{-1}$
bias voltage	3.0		V
f_{max}	1000		Hz
f_{min}	10		Hz
Clamped beam length	150	600	μm
Clamped beam width	60	60	μm
Clamped beam thickness	30	15	μm
Piezoresistor length	46	107	μm
Piezoresistor width	8	3	μm
Piezoresistor thickness	1.1	1.1	μm
Theoretical displacement sensitivity	77.1	7.1	μV/nm
Theoretical displacement resolution	0.19	4.6	nm
Theoretical displacement range limit	2.74	87.57	μm
Theoretical load range limit	444	27.75	mN

The maximum longitudinal stress is located on the surface of the beam roots which can be written as:

$$\sigma_{\text{l-max}} = \frac{3FL}{WD^2} \tag{12}$$

Where W is the width of the beam, and F is the force applied on the beam center. The sensors will fail when $\sigma_{\text{l-max}}$ equals to the bending strength (3.70 GPa, [3]) of (100) single crystal silicon. According to equation (12), the theoretical maximum forces that can be applied on the beam center and measured by the two sensors are calculated to be 444 mN for sensor A and 27.75 mN for sensor B, as listed in Table I. The force applied on the beam center, F, is given by:

$$F = \frac{2EWD^3x}{L^3} \tag{13}$$

Peer-reviewed version available at Micromachines 2017, 8, 31; doi:10.3390/mi8020031

Where x is the displacement of the beam center. According to equation (13), the maximum displacements of the two sensors are calculated to be 2.74 μm for sensor A and 87.57 μm for sensor B, as listed in Table 1. Therefore, the theoretical range limits of load and displacement that can be measured by the MEMS device are 27.75 mN and 2.74 μm, respectively.

3. Experiment

3.1. Fabrication process

Using bulk silicon micromachining process, the MEMS device was fabricated on a 4 inch (100) SOI (Silicon-On-Insulator) wafer, consisting of a 380 μm thick handle layer, a 60 μm thick n-type device layer with resistivity of 1~2 Ω·m and a 0.5 μm thick buried oxide layer. The minimum feature size of the device structure on the device layer is 6 μm. The device has an aspect ratio of 10. Fig. 5 shows the main steps of the fabrication process. First, a 300 nm thick SiO2 layers was grown on each side of the wafer by thermal oxidation as the insulation layer (Fig. 5a). The thermal oxidation SiO2 layer on the device side was patterned and etched as the mask for subsequent ion implantation. The piezoresistors, with resistivity of 1.17×10-2 Ω·cm, were prepared by boron doping by means of ion implantation at 100 keV with a dose of 1015 cm-2 (p- doped, Fig. 5b). Using the same process, electrical contacts were created with an implantation energy of 100 keV and a dose of 3×1015 cm-2 (p+ doped, Fig. 5c). An aluminum film of 1 μm thick was then sputtered on the surface and then etched using KOH solution to form interconnects and pads (Fig. 5d). The device layer was then etched by inductively coupled plasma (ICP) etching (Fig. 5e). Finally, ICP was used to etch the handle layer and the buried oxide layer out from the backside to create a movable structure (Fig. 5f). Fig. 6a shows a SEM image of a MEMS device fabricated. Fig. 6b shows a magnified view of sensor B. The corresponding lithography maps are shown in Fig. 6c and d. Comparison between the fabricated device and the lithography maps shows that the lateral undercutting of both ICP etching and aluminum film wet etching was less than 1 μm, indicating a well-controlled etching processes.

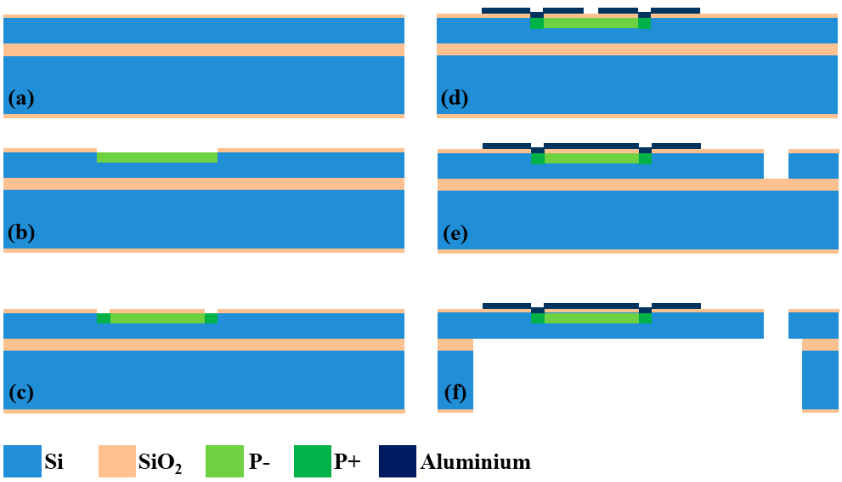

Figure 5. Schematic of the main steps to fabricate the MEMS device: (a) Thermal oxidation, (b) p-doped, (c) p+ doped and contact hole, (d) Interconnects and pads, (e) Front side ICP, (f) Structure release.

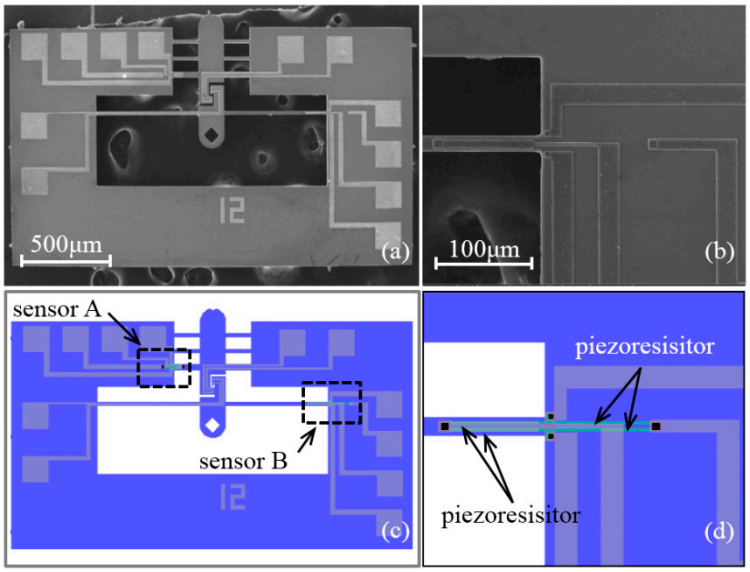

Figure 6. MEMS device with piezoresistive sensors: (a) SEM image of the device, (b) enlarged SEM image of the sensor B region, (c) Lithography map of the device, (d) Lithography map of the sensor B region.

3.2. Device calibration and quantitative tensile testing

A focused ion/electron dual-beam system (FIB/SEM, FEI Helios Nanolab 600i) was used to calibrate the displacement of the MEMS device in a high vacuum environment (10-5 Pa) with a purpose of avoiding the disturbances arising from variations in temperature, humidity, electromagnetic radiation and mechanical vibration, etc. [57, 58], as shown in Fig. 7a. Fig. 7b shows the design of the testing system setup for calibration. The MEMS device was first glued on to a custom-made printed circuit board (PCB) and then connected with the PCB by ultrasonic bonding. The PCB was then fixed onto a three dimensional micropositioner. The shuttle beam of the device was precisely aligned with the probe fixed on the piezo nanopositioner. The piezo nanopositioner moved in a step of 7 nm to drive the shuttle through the probe, ~10 μm in diameter. The displacement of the sample upon loading was measured from the SEM image taken. The corresponding output voltages of the displacement sensors were simultaneously measured by a multimeter. A voltage-displacement curve of the sensor was then obtained for displacement calibration.

Peer-reviewed version available at Micromachines 2017, 8, 31; doi:10.3390/mi8020031

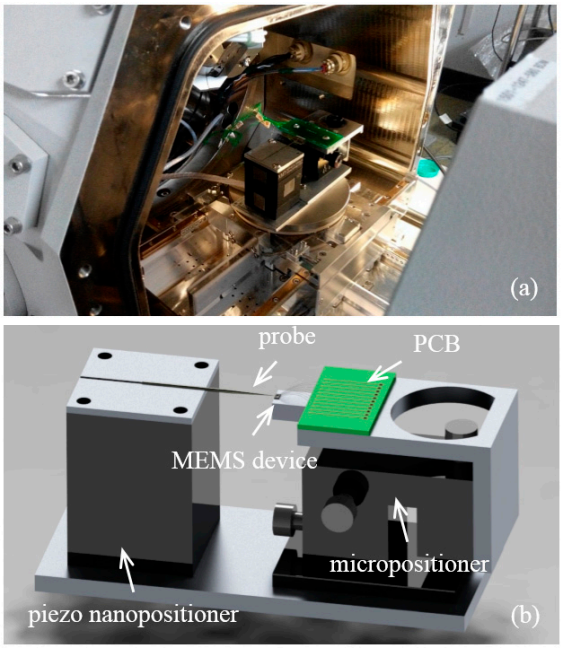

Figure 7. Setup for in-situ tensile testing in SEM; (a) The optical image of the testing system equipped in SEM, (b) Schematic of the testing system.

Using this testing system, uniaxial tensile tests were conducted on aluminum thin films in the FIB/SEM system. The original length of the specimen was measured from the SEM images. The displacement variance of the specimen upon loading was obtained by calculating the displacement difference of the two ends of the specimen, which were calculated from the output voltages of sensors A and B based on the voltage-displacement curve. The strain was calculated according to equation (1). The stress was calculated through equations (2) and (13) with cross-sectional area of the specimen measured from the surface and cross-sectional SEM images.

During the testing process, the piezo controller, power suppliers and mulitmeters, which were placed outside of the FIB/SEM system, were connected with the device and the nanopositioner inside FIB/SEM system through the flange of the SEM with shielded cables.

3.3. Specimen preparation

The accuracy of the testing system was tested by measuring the stress-strain curve of aluminum film sample with different thicknesses. The aluminum films for tensile testing were prepared by DC magnetron sputtering. The purity of the aluminum target is 99.99% and the sputtering parameters include working power 400 W, vacuum level 1.316×10-6 Pa and argon pressure 2~3 Pa. Aluminum film with thickness of ~1 μm was deposited on a thermally oxidized silicon wafer. Specimens for tensile testing in SEM was cut by FIB in the following sequence. First, a piece of the film was cut out with ion beam using a current of 9.4 nA, lifted out and moved to the specimen stages on the MEMS device with a W probe and fixed by Pt deposition on both ends. The film was then gradually thinned to hundreds of nanometers with ion beam at a series of currents of 9.4 nA, 2.3 nA, 0.77 nA and 7 pA

Peer-reviewed version available at Micromachines 2017, 8, 31; doi:10.3390/mi8020031

to minimize the damage caused by the incident ion beam. A specimen with thicknesses of 510 nm are shown in Fig. 8. The dimensions of the specimen are listed in Table 2.

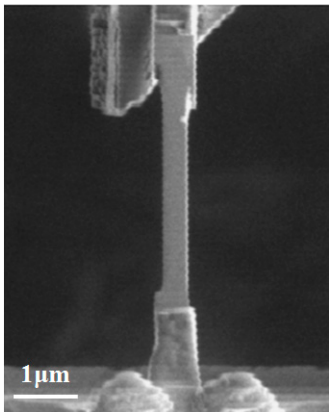

Figure 8. SEM image of a specimen fabricated for tensile testing.

Table 2. Dimensions of the Al specimen.

Length (nm)	Width (nm)	Depth (nm)
4880	620	510

4. Results and discussion

4.1. Sensors performance

Fig. 9 shows the current-voltage characteristics of the two piezoresistive sensors. It is seen that both sensors exhibited perfect linear behavior within the range of -5 ~ 5 V. This also indicates perfect contact between the sensors and the Al interconnects. The resistances of sensors A and B are determined to be 0.34 and 2.1 kΩ, respectively. Fig.10 shows the effect of bias voltage on the zero-point output voltage of the two sensors. It is seen that the zero-point output also has a linear dependence on the bias voltage for both sensors. The zero-point deviation can be attributed to the uneven ion implantation among the four resistors, despite the identical processing conditions used. Therefore, zero setting of the output voltage of the bridges was conducted on each sensor before the calibration.

Peer-reviewed version available at Micromachines 2017, 8, 31; doi:10.3390/mi8020031

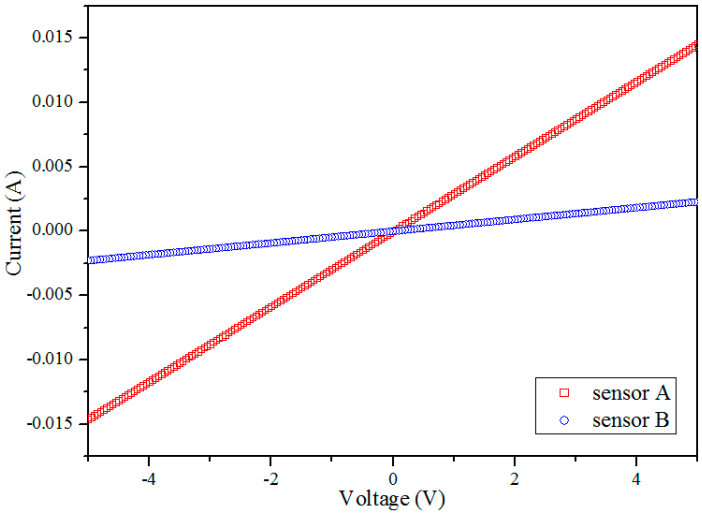

Figure 9. Current-voltage characteristics of the piezoresistors.

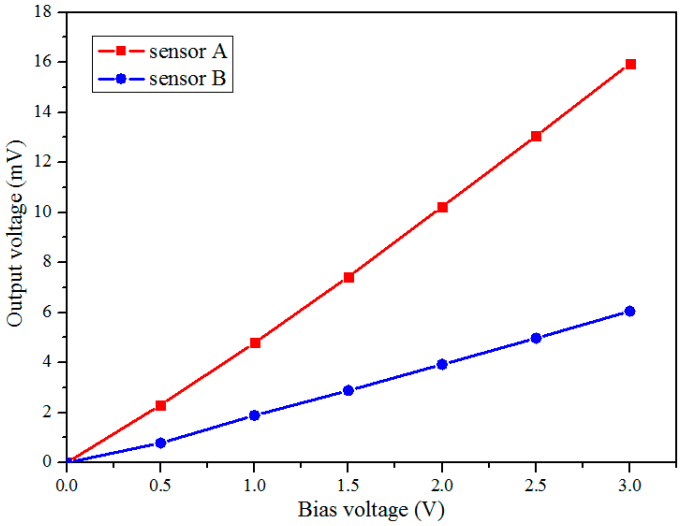

Figure 10. Zero-point deviation of the output voltage at different bias voltages.

Fig. 11 shows SEM images used to calibrate the displacements measured by sensors A and B. For each sensor, the center deflection of the beam, on which the sensor located, was obtained by measuring the distance variation between two reference points in SEM, i.e., points C and D for sensor A (Figs. 11a-f), and E and F for sensor B (Figs. 11g-l). The movements of beams A and B were driven by the piezo nanopositioner through the shuttle beam and the probe with a movement step size of 7 nm. Fig. 12 shows the output voltages of the two sensors versus the measured center deflection of the beams under a bias voltage of 3 V. It is seen that the sensor outputs are practically linear against the beam deflection. Using linear fitting, the displacement sensitivity is determined to be 37.4 μV/nm for sensor A and 4.8 μV/nm for sensor B. Comparing with the theoretical values listed in Table I, the deviations are 51.5% and 17.9% for the two sensors, respectively. This is commonly attributed to the non-uniformity of ion implantation and excess resistance in the bridge [59]. The linearities of sensors A and B are calculated to be 1.92% and 1.94%, respectively. Both values are smaller than the standard of a good linearity, 2%, demonstrating good sensor performance.

Preprints (www.preprints.org) | NOT PEER-REVIEWED | Posted: 30 December 2016 doi:10.20944/preprints201612.0147.v1

Peer-reviewed version available at Micromachines 2017, 8, 31; doi:10.3390/mi8020031

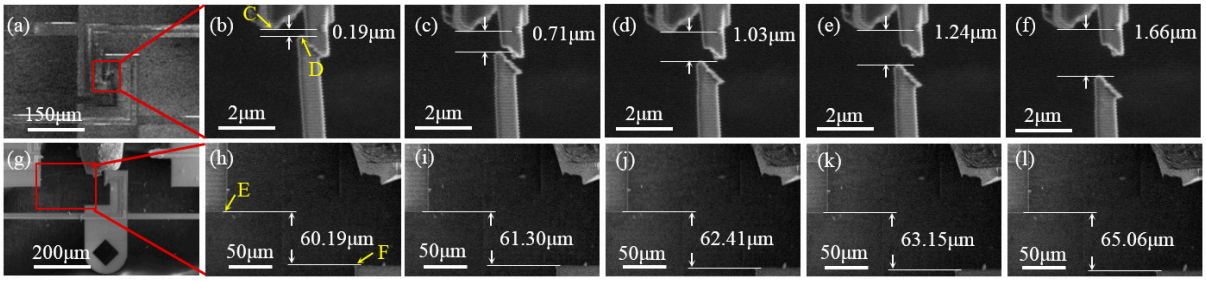

Figure 11. Displacement calibrations of sensors in SEM: (a)-(f) the displacement of two reference points for sensor A; (g)-(l) the displacements of reference points for sensor B.

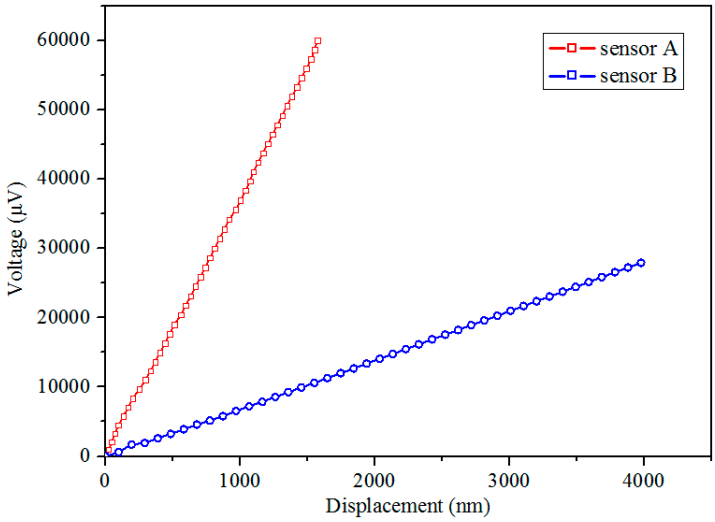

Figure 12. Output voltage as a function of the displacement.

The maximum displacement of the beam center achieved in this calibration is <5μm. This is far smaller than the beam length, thus the deflection can be treated as a linear system and described by the small deflection theory [60]. Therefore, we approximately take the stress defined by equation (12) as the load applied on the clamped beam. Based on the displacement sensitivities of sensors A and B and equation (10), the corresponding displacement resolutions are determined to be ~0.19 nm for sensor A and ~6.8 nm for sensor B. The sample elongation resolution is then determined to be 6.8 nm. The force resolution of sample /sensor B is then calculated to be 2.1 μN using equation (12). Since the displacements of sensors are measured by imaging method, the resolution that can be experimentally determined depends on the resolution of the SEM or TEM used. Further work on TEM is required to more accurately determine the displacement resolution.

Table 3. Sensitivity of the two sensors under irradiation of e-beams.

	Magnification		
	2000×	8000×	16000×

Peer-reviewed version available at Micromachines 2017, 8, 31; doi:10.3390/mi8020031

sensor A	37.5 μV/nm	37.2 μV/nm	37.4 μV/nm
sensor B	4.6 μV/nm	4.9 μV/nm	4.8 μV/nm

It is well known that the electron beam inside an electron microscope can lead to electron accumulation in the device, which may interfere with the sensor behavior. To assess the influence of electron beam on the displacement sensitivity of the sensors, sensors A and B were irradiated under the electron beam at an accelerating voltage of 2 kV (operating voltage) inside an SEM under magnifications of 2000, 8000 and 16000×. Table III shows the sensitivities of the sensors under irradiation of e-beam in SEM. The results show that no apparent changes of sensitivity can be detected, indicating a neglected influence of electron beam on sensor sensitivity.

4.2. Stress-strain curve

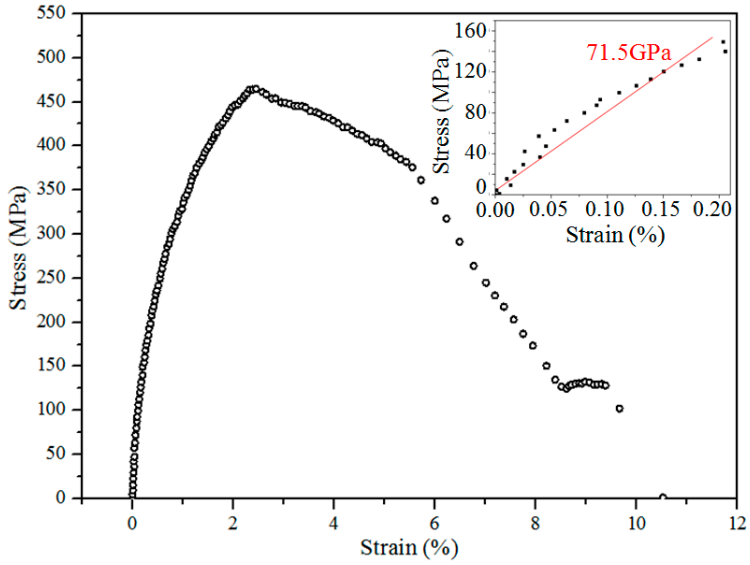

Figure 13. Stress-strain curve of an Al film with thickness of 510 nm.

An Al thin film of 510 nm in thickness was subjected to tensile deformation on the device in the FIB/SEM system with an actuation step size of 7 nm. SEM images were taken during tensile deformation. Fig. 13 shows the stress-strain curve measured of the Al film sample. The Young's modulus of the specimen is measured to be 71.5 GPa by linear fitting, consistent with bulk materials (68.5-71 GPa). The Young's modulus is also consistent with the 100 nm Al film measured by MEMS sensors [61]. The flow stress is determined to be ~460 MPa, which is lower compared to ~700 Mpa [61]. This may be related to the thickness and density of the film used.

5. Conclusions

A small sized MEMS device to quantitative study the mechanical properties of thin film materials *in situ* during TEM/SEM observation was designed and fabricated. The device was tested in SEM. Piezoresistive sensors were integrated on the device to quantitatively measure the mechanical

properties of materials. This device allows studies of microstructure-property correlations small materials and understanding of deformation mechanisms at nanometric and atomic scales. The main outcomes of this work may be summarized as follows:

(1) Sensors A and B have displacement sensitivities of 37.4 μV/nm and 4.8 μV/nm.

(2) Sensors A has a theoretical displacement resolution of 0.19 nm and sensors B has a force resolution of 2.1 μN.

(3) The MEMS device has a displacement range limit of 2.74 μm and a theoretical load range limit of 27.75 mN.

(4) Measurement of the Young's modulus of Al film by the device verify the reliability of the sensors.

(5) The device has a dimension small enough to be integrated on the TEM holder to study the property-structure correlation at the atomic scale.

Acknowledgments: This work was supported by NSFC (51231008, 11327901, 51001003), Beijing Nova program (2014B108), The Project of Construction of Innovative Teams and Teacher Career Development for Universities and Colleges under Beijing Municipality (IDHT20140504). S.C. Mao wishes to acknowledge the support of Internationalization Development Plan for Young Teachers of BJUT and Beijing Municipal Education Commission research project in grant KM201410005033, X.D. Han wishes to acknowledge the support of New Century Talents Project.

Author Contributions: Xiaodong Han, Shengcheng Mao and Ze Zhang conceived and designed the quantitative tensile experiments in SEM/TEM; Xiaodong Wang and Jianfei Zhang designed the MEMS device with piezoresistive sensors, carried out the performance tests of sensors and contributed simulations; Jin Ning contributed preparation of the device; Xudong Yang built the performance test system; Zhipeng Li, Qingsong Deng, Li Wang and Yuan Ji prepared the specimens; Shengcheng Mao and Xiaodong Wang analyzed the data; Xiaodong Han, Shengcheng Mao, Yinong Liu, Xiaodong Wang and Zhipeng Li wrote the paper. Conflicts of Interest: The authors declare no conflict of the interest. The founding sponsors had no role in the design of the study; in the collection, analyses, or interpretation of data; in the writing of the manuscript, and in the decision to publish the results.

Conflicts of Interest: The authors declare no conflict of interest.

References

1. Arzt, E., *Size effects in materials due to microstructural and dimensional constraints: a comparative review.* Acta Materialia, 1998. **46**(16): p. 5611-5626.
2. Tsuchiya, T., et al., *Specimen size effect on tensile strength of surface-micromachined polycrystalline silicon thin films.* Journal of Microelectromechanical Systems, 1998. **7**(1): p. 106-113.
3. Namazu, T., Y. Isono, and T. Tanaka, *Evaluation of size effect on mechanical properties of single crystal silicon by nanoscale bending test using AFM.* Journal of Microelectromechanical Systems, 2000. **9**(4): p. 450-459.
4. Sharpe, W.N., et al., *Effect of specimen size on Young's modulus and fracture strength of polysilicon.* Journal of Microelectromechanical Systems, 2001. **10**(3): p. 317-326.
5. Uchic, M.D., et al., *Sample Dimensions Influence Strength and Crystal Plasticity.* Science, 2004. **305**(5686): p. 986-989.
6. Greer, J.R., W.C. Oliver, and W.D. Nix, *Size dependence of mechanical properties of gold at the micron scale in the absence of strain gradients.* Acta Materialia, 2005. **53**(6): p. 1821-1830.
7. Parthasarathy, T.A., et al., *Contribution to size effect of yield strength from the stochastics of dislocation source*

lengths in finite samples. Scripta Materialia, 2007. **56**(4): p. 313-316.

8. Greer, J.R. and J.T.M. De Hosson, *Plasticity in small-sized metallic systems: Intrinsic versus extrinsic size effect.* Progress in Materials Science, 2011. **56**(6): p. 654-724.
9. Han, X.D., et al., *Low-Temperature in Situ Large Strain Plasticity of Ceramic SiC Nanowires and Its Atomic-Scale Mechanism.* Nano Letters, 2007. **7**(2): p. 452-457.
10. Han, X.D., et al., *Low-temperature in situ large-strain plasticity of silicon nanowires.* Advanced Materials, 2007. **19**(16): p. 2112-+.
11. Zhang, Y.F., et al., *Direct observation of super-plasticity of beta-SiC nanowires at low temperature.* Advanced Functional Materials, 2007. **17**(17): p. 3435-3440.
12. Zheng, K., et al., *Atomic Mechanisms Governing the Elastic Limit and the Incipient Plasticity of Bending Si Nanowires.* Nano Letters, 2009. **9**(6): p. 2471-2476.
13. Zheng, K., et al., *Electron-beam-assisted superplastic shaping of nanoscale amorphous silica.* Nature Communications, 2010. **1**: p. 24 (1-8).
14. Yue, Y.H., et al., *Approaching the Theoretical Elastic Strain Limit in Copper Nanowires.* Nano Letters, 2011. **11**(8): p. 3151-3155.
15. Li, H.X., et al., *An in situ TEM study of the size effect on the thermally induced martensitic transformation in nanoscale NiTi shape memory alloy.* Journal of Alloys and Compounds, 2014. **588**: p. 337-342.
16. Mao, S.C., et al., *Stress-induced martensitic transformation in nanometric NiTi shape memory alloy strips: An in situ TEM study of the thickness/size effect.* Journal of Alloys and Compounds, 2013. **579**: p. 100-111.
17. Han, X.D., et al., *In situ atomic scale mechanical microscopy discovering the atomistic mechanisms of plasticity in nano-single crystals and grain rotation in polycrystalline metals.* Ultramicroscopy, 2015. **151**: p. 94-100.
18. Wang, L., et al., *Grain rotation mediated by grain boundary dislocations in nanocrystalline platinum.* Nature Communications, 2014. **5**: p. 4402.
19. Wang, L.H., et al., *Direct Atomic-Scale Imaging about the Mechanisms of Ultralarge Bent Straining in Si Nanowires.* Nano Letters, 2011. **11**(6): p. 2382-2385.
20. Yue, Y.H., et al., *Quantitative Evidence of Crossover toward Partial Dislocation Mediated Plasticity in Copper Single Crystalline Nanowires.* Nano Letters, 2012. **12**(8): p. 4045-4049.
21. Wang, L.H., Z. Zhang, and X.D. Han, *In situ experimental mechanics of nanomaterials at the atomic scale.* Npg Asia Materials, 2013. **5**.
22. Wang, L.H., et al., *In Situ Observation of Dislocation Behavior in Nanometer Grains.* Physical Review Letters, 2010. **105**(13).
23. Jiang, Q.K., et al., *Super elastic strain limit in metallic glass films.* Scientific Reports, 2012. **2**.
24. Wang, L., et al., *Strongly enhanced ultraviolet emission of an Au@SiO2/ZnO plasmonic hybrid nanostructure.* Nanoscale, 2016. **8**(7): p. 4030-4036.
25. Kong, D.L., et al., *Reveal the size effect on the plasticity of ultra-small sized Ag nanowires with in situ atomic-scale microscopy.* Journal of Alloys and Compounds, 2016. **676**: p. 377-382.
26. Zang, K.T., et al., *Revealing ultralarge and localized elastic lattice strains in Nb nanowires embedded in NiTi matrix.* Scientific Reports, 2015. **5**.
27. Zhu, Y., C. Ke, and H.D. Espinosa, *Experimental techniques for the mechanical characterization of one-dimensional nanostructures.* Experimental Mechanics, 2007. **47**(1): p. 7-24.
28. Wang, B., V. Tomar, and A. Haque, *In-situ TEM mechanical testing of nanocrystalline zirconium thin films.* Materials Letters, 2015. **152**: p. 105-108.
29. Li, X., et al., *Nanoindentation of Silver Nanowires.* Nano Letters, 2003. **3**(11): p. 1495-1498.

30. Edwards, R.L., G. Coles, and W.N. Sharpe, *Comparison of tensile and bulge tests for thin-film silicon nitride.* Experimental Mechanics. **44**(1): p. 49-54.
31. Majjad, H., et al., *Dynamic determination of Young's modulus of electroplated nickel used in LIGA technique.* Sensors and Actuators A: Physical, 1999. **74**(1–3): p. 148-151.
32. Dzung Viet, D., et al., *Micro/nano-mechanical sensors and actuators based on SOI-MEMS technology.* Advances in Natural Sciences: Nanoscience and Nanotechnology, 2010. **1**(1): p. 013001.
33. Rui, L., et al., *A micro-tensile method for measuring mechanical properties of MEMS materials.* Journal of Micromechanics and Microengineering, 2008. **18**(6): p. 065002.
34. Warren, O.L., et al., *In situ nanoindentation in the TEM.* Materials Today, 2007. **10**(4): p. 59-60.
35. Bobji, M.S., et al., *A miniaturized TEM nanoindenter for studying material deformation in situ.* Measurement Science and Technology, 2006. **17**(6): p. 1324.
36. Pharr, G.M., *Measurement of mechanical properties by ultra-low load indentation.* Materials Science and Engineering: A, 1998. **253**(1 – 2): p. 151-159.
37. Wei, Y. and J.W. Hutchinson, *Hardness trends in micron scale indentation.* Journal of the Mechanics and Physics of Solids, 2003. **51**(11–12): p. 2037-2056.
38. Bucaille, J.L., et al., *Determination of plastic properties of metals by instrumented indentation using different sharp indenters.* Acta Materialia, 2003. **51**(6): p. 1663-1678.
39. Alkorta, J., J.M. Martínez-Esnaola, and J. Gil Sevillano, *Detailed assessment of indentation size-effect in recrystallized and highly deformed niobium.* Acta Materialia, 2006. **54**(13): p. 3445-3452.
40. Arsenlis, A. and D.M. Parks, *Crystallographic aspects of geometrically-necessary and statistically-stored dislocation density.* Acta Materialia, 1999. **47**(5): p. 1597-1611.
41. Busso, E.P., F.T. Meissonnier, and N.P. O'Dowd, *Gradient-dependent deformation of two-phase single crystals.* Journal of the Mechanics and Physics of Solids, 2000. **48**(11): p. 2333-2361.
42. Pantano, M.F., H.D. Espinosa, and L. Pagnotta, *Mechanical characterization of materials at small length scales.* Journal of Mechanical Science and Technology, 2012. **26**(2): p. 545-561.
43. Kumar, S., T. Alam, and A. Haque, *Quantitative in-situ TEM study of stress-assisted grain growth.* MRS Communications, 2013. **3**(02): p. 101-105.
44. Haque, M.A., H.D. Espinosa, and H.J. Lee, *MEMS for In Situ Testing—Handling, Actuation, Loading, and Displacement Measurements.* MRS Bulletin, 2010. **35**(05): p. 375-381.
45. Han, J.H. and M.T.A. Saif, *In situ microtensile stage for electromechanical characterization of nanoscale freestanding films.* Review of Scientific Instruments, 2006. **77**(4): p. 045102.
46. Jin, Q.H., et al. *In-situ TEM tensile test of 90nm-thick SCS beam using MEMS chip*. in *Sensors, 2008 IEEE*. 2008.
47. Yu, S. and J.N. Bradley, *MEMS capacitive force sensors for cellular and flight biomechanics.* Biomedical Materials, 2007. **2**(1): p. S16.
48. Dongfeng, Z., et al., *Electron Microscopy Mechanical Testing of Silicon Nanowires Using Electrostatically Actuated Tensile Stages.* Microelectromechanical Systems, Journal of, 2010. **19**(3): p. 663-674.
49. Barlian, A.A., et al., *Review: Semiconductor Piezoresistance for Microsystems.* Proceedings of the IEEE, 2009. **97**(3): p. 513-552.
50. Tortonese, M., R.C. Barrett, and C.F. Quate, *Atomic resolution with an atomic force microscope using piezoresistive detection.* Applied Physics Letters, 1993. **62**(8): p. 834-836.
51. Duc, T.C., J.F. Creemer, and P.M. Sarro, *Lateral nano-Newton force-sensing piezoresistive cantilever for microparticle handling.* Journal of Micromechanics and Microengineering, 2006. **16**(6): p. S102.

52. Chui, B.W., et al., *Advanced temperature compensation for piezoresistive sensors based on crystallographic orientation.* Review of Scientific Instruments, 2007. **78**(4): p. 043706.
53. Smith, C.S., *Piezoresistance Effect in Germanium and Silicon.* Physical Review, 1954. **94**(1): p. 42-49.
54. Kanda, Y., *Piezoresistance effect of silicon.* Sensors and Actuators A: Physical, 1991. **28**(2): p. 83-91.
55. Taechung, Y. and K. Chang-Jin, *Measurement of mechanical properties for MEMS materials.* Measurement Science and Technology, 1999. **10**(8): p. 706.
56. Harkey, J.A. and T.W. Kenny, *1/f noise considerations for the design and process optimization of piezoresistive cantilevers.* Microelectromechanical Systems, Journal of, 2000. **9**(2): p. 226-235.
57. Nakladal, A., K. Sager, and G. Gerlach, *Influences of humidity and moisture on the long-term stability of piezoresistive pressure sensors.* Measurement, 1995. **16**(1): p. 21-29.
58. Hoa, P.L.P., G. Suchaneck, and G. Gerlach, *Influence of polycrystalline silicon as electrical shield on reliability and stability of piezoresistive sensors.* Sensors and Actuators A: Physical, 2005. **120**(2): p. 567-572.
59. Park, S.J., J.C. Doll, and B.L. Pruitt, *Piezoresistive Cantilever Performance-Part I: Analytical Model for Sensitivity.* J Microelectromech Syst, 2010. **19**(1): p. 137-148.
60. Rob, L., A.W. Groeneveld, and M. Elwenspoek, *Comb-drive actuators for large displacements.* Journal of Micromechanics and Microengineering, 1996. **6**(3): p. 320.
61. Haque, M.A. and M.T.A. Saif, *Application of MEMS force sensors for in situ mechanical characterization of nano-scale thin films in SEM and TEM.* Sensors and Actuators A: Physical, 2002. **97–98**: p. 239-245.